Journal of Sound and Vibration (1999) **227**(5), 1049–1081
Article No. jsvi.1999.2395, available online at http://www.idealibrary.com on IDEAL®

ON CONTACT-INDUCED STANDING WAVES IN ROTATING TIRES: EXPERIMENT AND THEORY

ANINDYA CHATTERJEE, JOSEPH P. CUSUMANO AND JOHN D. ZOLOCK†

Department of Engineering Science and Mechanics, The Pennsylvania State University, 227 Hammond Building, University Park, PA 16802, *U.S.A.*

(*Received* 6 *August* 1998, *and in final form* 17 *May* 1999)

An experimental and theoretical study of standing waves in a rotating tire is presented. A test set-up for studying small balloon tires is described. Experimental observations of standing waves arising after a critical speed transition are presented, including measurements of the spatial structure of the standing waves. A simple model for the tire is developed, which has a single degree of freedom at each radial location. Steady state solutions at any rotation speed are governed by a non-linear boundary value problem, which is studied in detail. Appropriate boundary conditions are obtained using asymptotic arguments, and then used in numerical solutions. The analysis is shown to agree well with the experimental observations. Based on the analysis, a method for suppressing the standing waves is proposed and confirmed experimentally.

1. INTRODUCTION

The phenomenon of standing waves in tires, which occur when the tire rotates faster than some critical speed, has been the subject of many papers. In addition to its intrinsic interest as a problem in the dynamics of solids, the critical speed phenomenon represents a serious performance limitation for high-speed vehicles, since the large strains associated with the standing waves invariably lead to significant working of the tire material and hasten tire failure. Useful reviews can be found in reference [1], which covers work prior to 1970, as well as in reference [2], which brings together many issues related to tires, from materials to dynamics.

Theoretical work relevant to vibrations and waves in tires ranges from analytical or combined numerical/analytical studies of continuum equations for ring-type models [3–12], toroidal membrane models [13] and thin shell models [14], to numerical studies using finite elements [15–20]. Experimental studies have predominantly dealt with the modal analysis of non-rotating tires [6, 11, 21–23]. Dynamic stiffnesses have been evaluated experimentally on a small-scale tire [3],

† Present address: Volpe National Transportation Systems Center, Kendall Sq., Cambridge, MA 02142.

0022-460X/99/451049 + 33 $30.00/0

and full-scale dynamometer test rigs have been used to determine critical speeds on aircraft tires [19, 24, 25]. In reference [25], a sensitive Moiré fringe technique was used to visualize the formation of standing waves and hence determine the critical speed. Finally, in reference [26], a tire modelled as a tensioned band on a viscoelastic foundation was examined at speeds well below the critical speed to investigate the effects of damping on rolling resistance.

In this paper, we present a combined experimental and theoretical study of tire standing waves in perhaps the simplest type of peneumatic tire. In the literature, standing waves have been interpreted variously (and somewhat confusingly) as resulting from shocks, resonances, or instabilities. Based on our experiments and an asymptotic analysis of our model, we find none of these interpretations to be completely satisfactory. We find, however, that the appearance of standing waves does *approximately coincide* with the appearance of a shock at the leading edge of contact, for the balloon tires studied here (though the shock neither causes, nor has any influence on, the standing wave). Small amounts of shear dissipation and/or flexural rigidity destroy the sharpness of (or "regularize") the shock. The resonance interpretation succeeds in predicting the correct critical speed, but several other aspects of the system behavior are not consistent with the usual view of resonance. The instability interpretation does not seem meaningful because there is no non-oscillatory solution (i.e., without a standing wave) that loses stability to give rise to the standing wave solution: when the oscillatory solution appears, the non-oscillatory solution ceases to exist.

The first part of this paper deals with experiments run on an inexpensive tire test rig designed and built in our laboratory to run small (4·5 in or 11·43 cm in diameter) pneumatic balloon tires. Images grabbed from live video are processed to extract the spatial structure of standing waves observed in the tires. Spatial frequencies and spatial attenuation rates for the standing wave are estimated for four different tire pressures, and the results are shown to be in good qualitative agreement with numerical results of previous researchers.

In the second part of this paper, we present a simple model for the rotating balloon tire with ground contact. Normally, one might think that only membrane effects would be important in the study of balloon tires. However, as we show in the analysis, the small amount of flexural rigidity present in real balloon tires is important for understanding the structure of the observed standing waves. Steady standing wave solutions at any fixed speed are governed by a non-linear boundary value problem, which is analyzed in detail using singular perturbation methods. The qualitative predictions of the model compare quite well with the experimental observations. Furthermore, the utility of the model is demonstrated by a final experiment in which it is shown how it is possible to suppress the standing waves.

The analytical treatment of standing waves presented here is different from other studies in the literature which interpret results using natural frequencies and mode shapes [10], or which use wave propagation ideas [13], in that we explicitly and analytically formulate the non-linear boundary value problem associated with steady state rolling conditions. The model captures the essential qualitative behavior of radial displacements of the rotating tire crown, even though it is not as detailed as, say, finite element models (see, e.g., references [16, 18]). The present

version of the model might be less appropriate for tires which have substantial flexural rigidity. For such tires, ring-on-elastic-foundation type models (see, e.g, references [8, 9]) might be more effective, or at least quantitatively more accurate. Nevertheless, consideration of our model provides substantial insight into the fundamental mechanics of contact-induced standing waves in rotating axisymmetric systems. Such insight is often obscured by more detailed, usually numerical, models. Furthermore, the approach presented in this paper can, in principle, be extended to more general cases.

The rest of this paper is organized as follows. Sections 2 and 3 describe the experimental set-up and our experimental observations. Sections 4–8 present a simple model for the tire, and a detailed analysis of the model including qualitative comparisons with experimental results. In Section 9, we discuss the question of the physical origin of standing waves in dissipative tires. Section 10 describes a final experiment that demonstrates the possibility of suppressing the standing waves, as predicted by the model. Finally, in Section 11, we present our conclusions.

2. EXPERIMENTAL SET-UP

The apparatus shown in Figure 1 was used to study small balloon tires of the type used for large-scale radio-controlled model aircraft. The toroidal tires have a diameter of 11·43 cm (4·5 in), and a nominal wall thickness of 0·127 cm (0·05 in). The tire is mounted on a hub which is itself mounted directly on a motor shaft. This

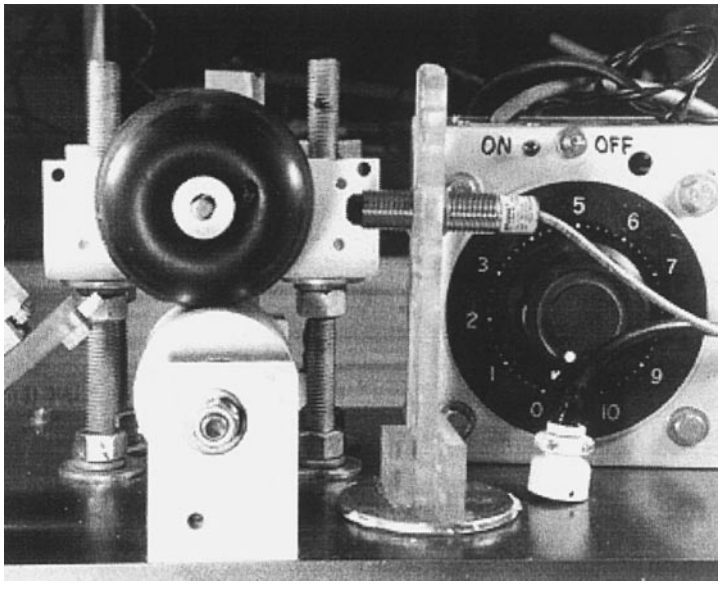

Figure 1. The test rig with ballon tire mounted above the flywheel. The infrared thermocouple and manual speed control are visible to the right of the tire. An optical displacement probe is visible at lower left.

direct drive arrangement allows for rapid tire changes between experiments. The motor is a 10 000 rpm or 167 Hz (max) permanent magnet unit with a maximum torque of 0·353 N m (3·125 in lb) at 5·5 A. The tire makes contact with a 7·62 cm (3·0 in) diameter solid aluminum flywheel mounted on ball bearings. The distance between the motor shaft centerline and flywheel surface is fixed at 4·62 cm (1·82 in). The speed of the motor is controlled manually using a Variac.

An optical infrared thermocouple with a sensitivity of $\pm 0{\cdot}5^{\circ}C$ is used to measure the temperature at a location along the circumference of the tire with a spatial resolution of about 2·5 cm (1 in). An optical displacement probe can be used to monitor surface vibrations of the tire at various locations around the circumference of the tire. All sensor output is low-pass filtered and acquired by a 12-bit data acquisition system, with a maximum aggregate 100 kHz data rate. A digital encoder used to measure tire angular velocity outputs 4 pulses per revolution, which provides an accuracy of about 0.3% or better in the speed range of interest.

A CCD camera coupled to a video frame grabber is used to obtain quantitative measurements of tire shapes at various speeds. Video images taken with the line of sight along the axis of tire rotation are captured digitally to look at tire motions frame by frame. The captured images are processed to extract the tire boundary for further analysis, allowing, for example, standing wave wavelength and spatial attenuation rates to be estimated. The current video system is suitable only for studying steady standing wave patterns: it does not have the frame rate needed to study the transient dynamics of the tire.

This experimental set-up is inexpensive and quite convenient for studying tire standing waves: power requirements are low, the system is quiet, and thus the data is relatively clean. Furthermore, the relatively low energies involved in spinning up the small-scale tires makes the system quite safe.

3. EXPERIMENTAL OBSERVATIONS

Experiments were conducted on tires inflated to pressures of 10·3, 15·5, 20·7, and 25·9 kPa (1·5, 2·25, 3·0, and 3·75 psi). For each fixed pressure, runs were started with a new tire at rest and ambient temperature. The motor speed was increased in small increments and held until the short-term mechanical (but, as discussed below, not necessarily thermal) steady state was reached. Video images were then obtained using the frame grabber. At the same time, vibration and temperature data were automatically collected for later use, as needed. This procedure was repeated until each tire failed, usually in about 20 steps. The time required to run each tire through the entire process ranged from about 300 to 500 s. During the procedure, the transition through the critical speed and the development of standing waves are clearly visible. Once standing waves have developed, the tires undergo significant deformation before failure, as can be seen by overlaying video images at low and high speeds, as shown in Figure 2 (left). However, despite the large deformations involved, the displacements of the tire crown remain predominantly radial, as shown in Figure 2 (right).

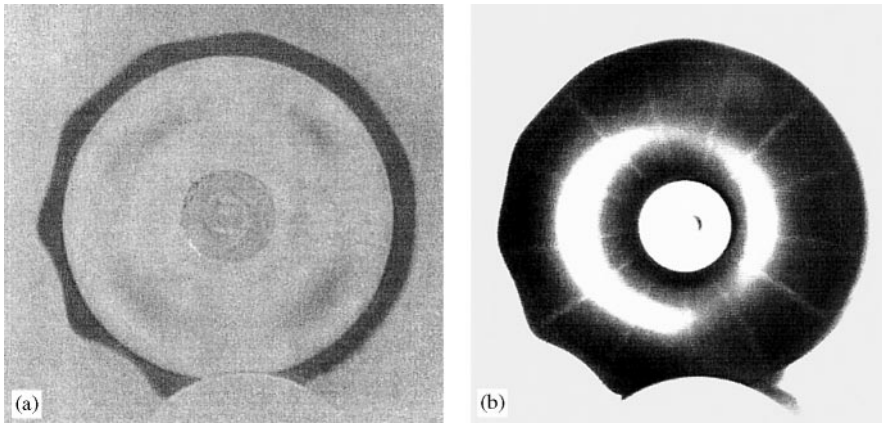

Figure 2. Deformation kinematics after the onset of standing waves: (a) overlay of images taken at rest and above the critical speed, showing the magnitude of tire deformations and the increase in the contact patch area; (b) image taken with a strobe, showing that a white radial line on the tire remains approximately straight and radial as it rotates. The tires in both figures are rotating clockwise.

Image processing software was used to process the raw 240×360 pixel, 8-bit color video images. After converting the images to grey scale and performing a contrast enhancement to make the tire boundary stand out, edge detection software was used to extract the tire boundary and store it on disk. At this point, the data consist of a relatively small number of individual (x, y) pairs located in a 240×360 grid. Figure 3 shows the results for rotation speeds below and above the critical speed for the 15·5 kPa (2·25 psi) initial pressure case.

By locating the center of the wheel, the data can be transformed into polar co-ordinates. After low-pass filtering the results to eliminate noise caused by the pixelization and camera/tire jitter, the spatial data can be presented in the waterfall plot of Figure 4. Plotted this way, the variation in the amplitude, wavelength, and spatial attenuation of the large-amplitude standing waves just after the contact patch can be seen as a function of tire angular velocity. The results shown in Figure 4 are qualitatively similar to the finite element solutions obtained in references [15, 16]. An apparently special feature of standing waves in balloon tires, seen in the plots, is the appearance of small amplitude "ripples" just *ahead* of the contact patch. These ripples are most clearly visible just below the speed at which large-amplitude standing waves appear, but are not so clearly present at substantially higher speeds.

By directly using the pixel data, the global deformation properties of the tires can be computed. In Figure 5, the average tire radius and average circumferential strain (relative to the zero velocity configuration) are shown as a function of tire angular velocity. We remark that the shapes of the curves can be qualitatively understood merely by considering the dynamics of a single sprung mass attached to a rotating base. This observation, together with the observation of essentially radial displacements of the tire crown, motivate the model developed in the next section.

To obtain a simple quantitative measure of the spatial properties of the standing waves, the standing wave patterns of Figure 4 were fast Fourier transformed, and

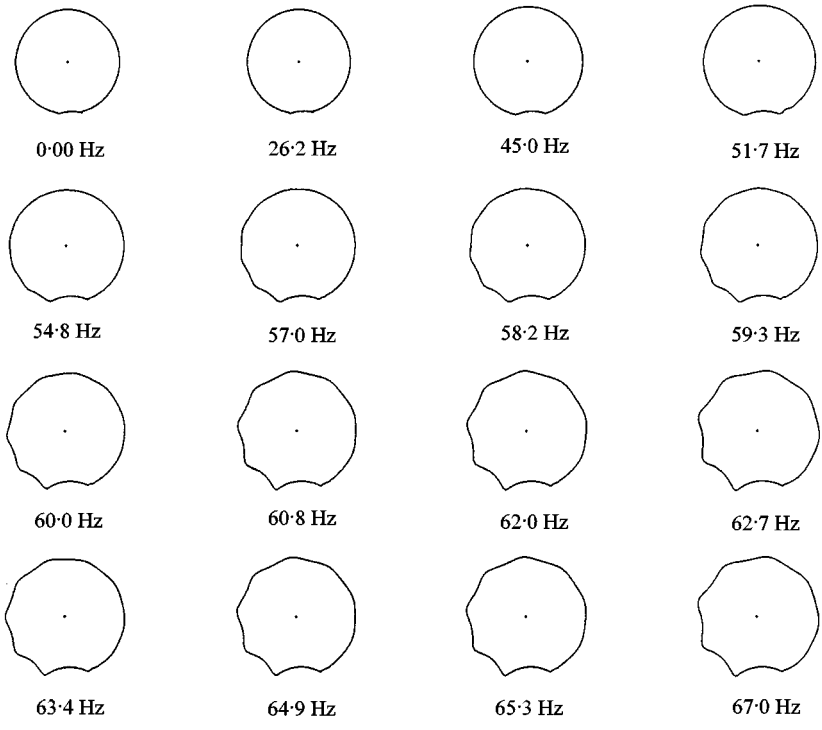

Figure 3. Tire shapes extracted from video data for the case with initial pressure equal to 15·5 kPa (2·25 psi). The tire is rotating clockwise.

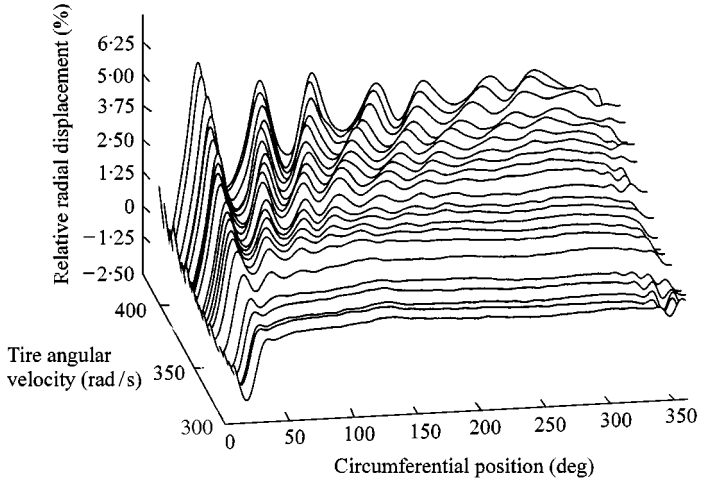

Figure 4. Waterfall plot showing the development of standing waves as tire angular velocity increases for the 15·5 kPa (2·25 psi) initial pressure case. All displacements are given relative to the average tire radius (see Figure 5) for a given speed. The region from the minimum in each plot near the 20° position on the tire circumference to the next maximum on either side is the contact patch.

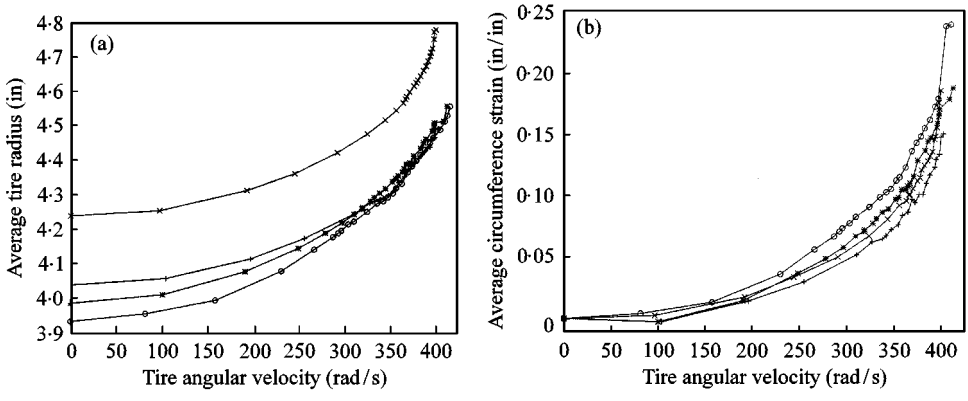

Figure 5. Global deformation versus tire angle velocity: (a) average radial displacement of the tire crown; (b) average circumferential strain relative to rest configuration. The symbols represent the different initial pressures in kPa (psi); ○, 10·3 (1·5); * 15·5 (2·25); + 20·7 (3·0); × 25·9 (3·75).

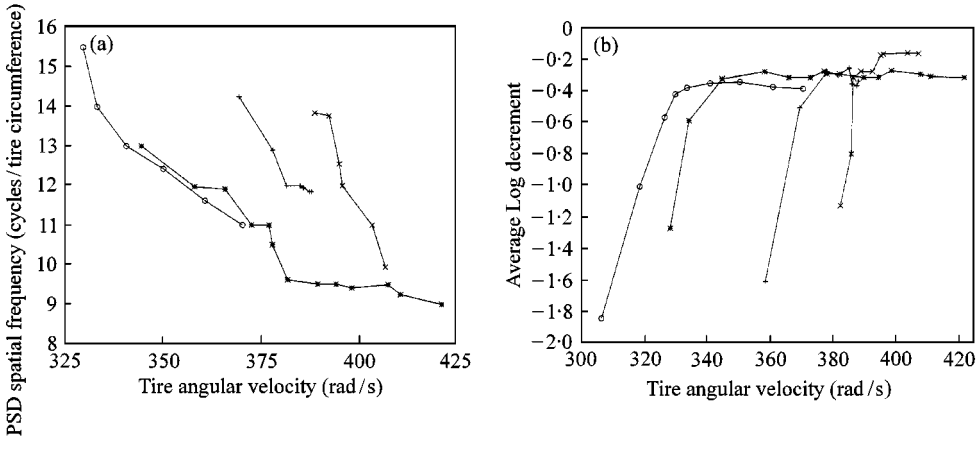

Figure 6. Spatial characteristics of tire standing waves: (a) average spatial frequency vs. tire angular velocity; (b) measure of spatial attenuation of the standing waves using the average logarithmic decrement. See Figure 5 for symbol legend. Each curve starts just past the corresponding critical speed.

the first peak was taken to be the characteristic spatial frequency for each tire speed. The first speed at which this peak exceeded a fixed threshold was taken to define the critical speed experimentally. Figure 6 shows that the characteristic spatial frequency of the standing waves decreases with the tire angular velocity, and that the rate of this decrease is larger for higher pressures. This is qualitatively in agreement with earlier numerical work, particularly reference [15]. A simple measure of the spatial attenuation rate of the standing waves was obtained using the average logarithmic decrement of successive peak-to-peak amplitudes in the standing waves. In Figure 6 we see that at all pressures the attenuation is high right after the critical velocity, but drops off in magnitude (i.e., becomes less negative) as the angular velocity is increased.

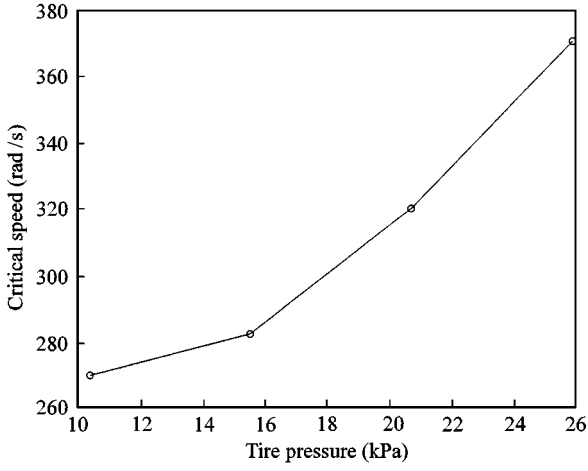

Figure 7. Critical speed for the onset of standing waves as a function of initial inflation pressure.

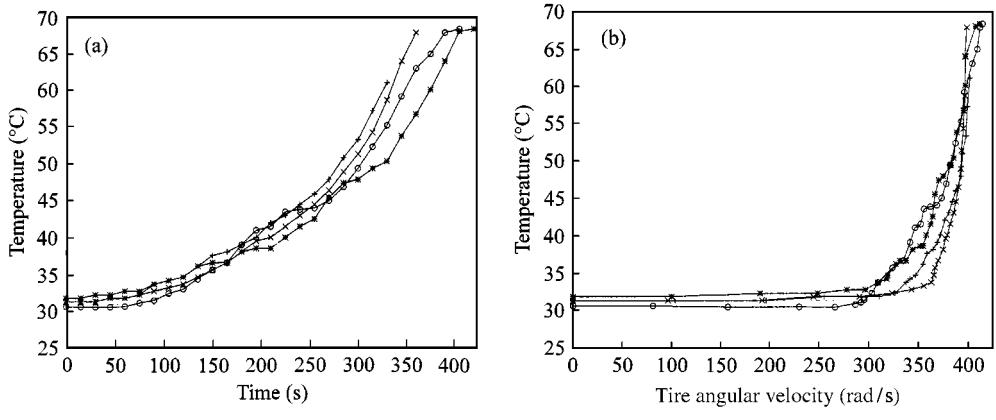

Figure 8. Temperature just after the contact patch: (a) temperature versus time; (b) temperature versus angular velocity for the same pressures. In the latter figure, the sharp rise in temperature just after the critical speed is readily apparent in the figures. See Figure 5 for symbol legend.

The resulting critical speeds are shown in Figure 7 for all four tire pressures. That the critical speed is found to be an increasing function of tire pressure is not surprising in the light of earlier work that related the critical speed to the natural frequencies of the tire [12, 15, 16, 20], in that increased internal pressure raises the eigenfrequencies. However, as we will discuss later, contact-induced standing waves are not clearly interpretable as resonance phenomena.

As mentioned earlier, the procedure used during most of the experimental runs did not consider the time necessary for the tire to reach thermal equilibrium. This was done in order to allow large deformation data to be collected before the tire failed. Nevertheless, despite this lack of direct control over the thermal history of each specimen, the experiments were carried out with sufficient consistency to keep the time–temperature histories for the various runs approximately the same, as shown by the data in Figure 8 (left). Further insight into the mechanical

consequences of the standing waves can be obtained by plotting the temperature as a function of tire angular velocity. As shown in Figure 8 (right), the tire temperatures remain approximately constant (at room temperature) until just after the critical speed, whereupon the temperature is seen to rise dramatically with increasing speed due to the large amount of work put into the tire material by the standing-wave-induced strain cycles. Note that for all of the temperature data shown, the infrared thermocouple was aimed just after the contact patch, at the portion of the tire which has just been released from the flywheel.

We conclude this section by summarizing the essential qualitatives features of the standing wave phenomena as follows:

(1) As the steady rotation speed is increased, the tire expands radially. The size of the contact region grows.
(2) Past some critical speed, small-amplitude, small-wavelength, standing waves ("ripples") are formed near the *leading edge* of the contact region, i.e., "ahead" of the contact patch. The amplitudes of these waves decay rapidly with increasing distance from the leading edge.
(3) At a slightly higher speed, larger standing waves appear near the *trailing edge* of the contact region, i.e., "behind" the contact patch. These waves have amplitudes that decay with increasing distance from the trailing edge at a rate significantly lower than that of the ripples.
(4) As the rotation speed is further increased, the amplitude and wavelength of the trailing edge standing waves *increases* while the spatial decay rate along the circumference *decreases*.
(5) Throughout each experiment, radial sections in the tire remain radial to a good approximation, as shown in Figure 2. The temperature of the tire rises steadily with speed, until the tire eventually fails.

4. MODEL FORMULATION

We now present a model for the system examined in the previous sections. This model is a simplification of the toroidal membrane model of reference [13], in that a single-mode approximation is used for the displacements in any given radial plane. The model may also be thought of as the continuum limit of the system shown schematically in Figure 9. The kinematic assumption of purely radial displacements is supported by our observations of the experimental system (recall Figure 2 (right)). As in the experimental system, the center of the rotating wheel is assumed to be held at a fixed height h above the ground. For simplicity, here we assume that $h = R$, the undeformed tire radius. In a co-ordinate system fixed to the tire, this system may be described by the partial differential equation

$$\bar{\rho}\bar{u}_{\bar{\tau}\bar{\tau}} - \bar{\rho}\bar{\omega}^2 (R + \bar{u}) = -\bar{k}\bar{u} - \bar{\zeta}_1 \bar{u}_{\bar{\tau}} + \bar{K}\bar{u}_{\theta\theta} + \bar{\zeta}_2 \bar{u}_{\theta\theta\bar{\tau}} - \bar{P}(\theta, \bar{\tau}), \tag{1}$$

where $\bar{u}$ is the radial displacement (positive outwards), θ is the angular position on the tire, $\bar{\tau}$ is time, and the θ and $\bar{\tau}$ subscripts denote partial derivatives. The various parameters have the following physical significance: $\bar{\rho}$ is the effective mass per unit

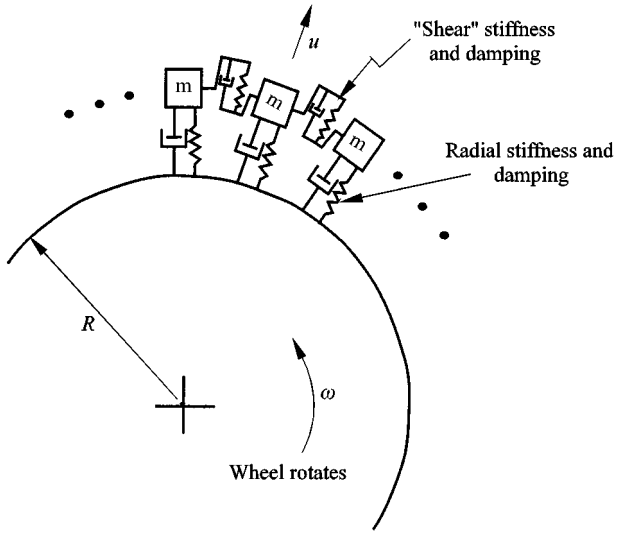

Figure 9. Schematic diagram motivating the continuum model of equation (1) (radial displacements only).

angle (θ), R is the nominal radius of the undeformed tire, $\bar{k}$ is the resistance to purely radial deformation (or "radial stiffness"), $\bar{K}$ is the resistance to relative radial deformation (or "shear stiffness"), $\bar{\zeta}_1$ is the viscous resistance to purely radial motions ("radial damping"), $\bar{\zeta}_2$ is the viscous resistance to relative radial motions ("shear damping"), and $\bar{\omega}$ is the angular velocity of the tire. $\bar{P}$ represents any externally applied, radially directed, distributed force ($\bar{P}$ is taken to be positive when it is radially inwards).

Note that the sign conventions for $\bar{u}$ (positive outwards) and $\bar{P}$ (positive inwards) are in accordance with the physical situation (the tire expands outwards, while the contact force acts inwards). An obvious consequence of this is that (see equation (1)) for a non-rotating tire with a uniform *positive* external loading $\bar{P}_0$ acting on its entire circumference, the steady state solution $\bar{u} = -\bar{P}_0/\bar{k}$ is negative.

By non-dimensionalization of equation (1), we obtain

$$u_{\tau\tau} - \omega^2 (1 + u) = -u - \zeta_1 u_\tau + K u_{\theta\theta} + \zeta_2 u_{\theta\theta\tau} - P(\theta, \tau), \tag{2}$$

where the new non-dimensional variables and parameters are

$$u = \frac{\bar{u}}{R}, \quad \tau = \sqrt{\frac{\bar{k}}{\bar{\rho}}}\,\bar{\tau}, \quad P = \frac{\bar{P}}{R\bar{k}}, \quad \omega = \sqrt{\frac{\bar{\rho}}{\bar{k}}}\,\bar{\omega}, \quad \zeta_1 = \frac{\bar{\zeta}_1}{\sqrt{k\bar{\rho}}}, \; \zeta_2 = \frac{\bar{\zeta}_2}{\sqrt{\bar{k}\bar{\rho}}} \text{ and } K = \frac{\bar{K}}{\bar{k}}.$$

The distributed contact force $P(\theta, \tau)$ we will consider is that arising from the contact between the rotating tire and the rigid ground. It is actually an unknown constraint force. In other words, in the non-contact region, $P \equiv 0$, while in the contact region, the shape of the ground (i.e., the constraint) determines P.

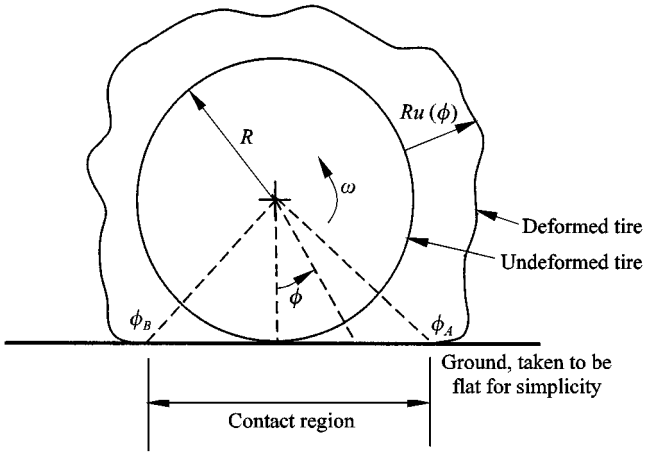

Figure 10. The contact region.

Since we are interested in steady, standing wave solutions, we now introduce new co-ordinates

$$\phi = \theta + \omega\tau \quad \text{and} \quad t = \tau.$$

In this new lab-fixed co-ordinate system, steady standing wave solutions are those that are independent of time t. Such solutions satisfy the ordinary differential equation

$$\zeta_2\,\omega u_{\phi\phi\phi} + (K - \omega^2)u_{\phi\phi} - \zeta_1\,\omega u_\phi - (1 - \omega^2)u + \omega^2 = P(\phi). \tag{3}$$

Outside the contact region, u is described by equation (3) with $P(\phi) \equiv 0$. Inside the contact region, u is given by

$$u(\phi) = \sec\,\phi - 1 \tag{4}$$

(see Figure 10), and $P(\phi)$, which must satisfy $P \geqslant 0$, can be found by substituting the known $u(\phi)$ of equation (4) into equation (3). Finding the endpoints of the contact region (see Figure 10) is part of the problem at hand. We assume that contact occurs over a single, connected region, i.e., we do not seek solutions where contact occurs over two or more disjoint intervals.

Note that equation (3) is linear when restricted to either the contact region or the non-contact region, although steady standing wave solutions of the system are described by a non-linear boundary value problem: the non-linearity arises because the extent of the contact region is not known in advance, depends on the as yet undetermined solution u, and varies with the angular velocity ω (i.e., the problem has a "free boundary").

One might initially suppose that $P = 0$ at one or both edges of the contact region. That this need not be true may be seen from considering the static (non-rotating) solution for the case when the tire is pressed by an amount δ into the ground. In that case, $u(\phi) = (1 - \delta)\sec\,\phi - 1$ in the contact region, while outside the contact

region $P \equiv 0$ and u satisfies the second-order ordinary differential equation obtained by setting $\omega = 0$ in equation (3). For small δ, the size of the contact region is also small. It is easy to show that in this small contact region, the distributed contact force $P \approx K > 0$. Thus, for slow enough rotation speeds (i.e., small enough ω), we expect P to be strictly positive at each edge of the contact region.

When the tire rotates with large enough ω, it is possible that P might be zero at a boundary point. On the other hand, P might also develop a concentrated force with the form of a delta function at a boundary point. We demonstrate later in this paper that both of these cases do occur. (A concentrated force is assumed to exist at an edge of the contact region only if no solution can be found without one.)

We now examine the nature of solutions to the non-linear boundary value problem as a function of the rotational velocity ω. In Sections 5 and 6, we study the cases of zero and non-zero shear damping respectively. In Section 7, we discuss the effects of a small amount of flexural rigidity in the tire. In Section 8, we qualitatively compare predictions of the model and experimental observations.

5. THE ZERO SHEAR DAMPING CASE

We first consider the case where the shear damping $\zeta_2 = 0$. We assume that the radial damping $\zeta_1 > 0$. Equation (3) becomes

$$(K - \omega^2)u_{\phi\phi} - \zeta_1 \omega u_\phi - (1 - \omega^2)\, u + \omega^2 = P(\phi). \tag{5}$$

A similar equation appears in reference [26], except for a missing "centrifugal" effect which we include here.

In equation (5), we assume $K < 1$, since from a simple static deflection test (described in the next section) we estimated K for our tire to be about 0·12. Moreover, as shown in reference [13], for example, K is expected to be roughly proportional to the square of the ratio of the cross-section radius to the radius of the tire, so $K < 1$ seems generally reasonable for balloon tires.

In equation (5), the coefficient of the highest derivative change sign as ω passes through $\sqrt{K}$. We now examine the nature of solutions as ω passes through this critical value, $\omega_c = \sqrt{K}$. (We will show later that standing waves actually appear at a slightly higher speed than ω_c. In an experimental context, the critical speed is taken to be the speed at which standing waves are first detectable. However, for purposes of analysis, we take ω_c as "the" critical speed. The two speeds are the same in the limit of small damping.)

5.1. CHARACTERISTIC EQUATION

Equation (5) is a linear, constant coefficient equation. In the non-contact region, it has solutions of the form

$$u(\phi) = \frac{\omega^2}{1 - \omega^2} + C_1 \mathrm{e}^{r_1 \phi} + C_2 \mathrm{e}^{r_2 \phi}, \tag{6}$$

where r_1 and r_2 satisfy

$$(K-\omega^2)r^2-\zeta_1\omega r-(1-\omega^2)=0. \tag{7}$$

The roots of the above quadratic equation are

$$r_{1,2}=\frac{\zeta_1\omega\pm\sqrt{\zeta_1^2\omega^2+4(K-\omega^2)(1-\omega^2)}}{2(K-\omega^2)}. \tag{8}$$

Note that the above expression allows a simple static indentation test to be used to estimate K, since for $\omega=0$, the characteristic equation for equation (5) above has roots $\pm 1/\sqrt{K}$.

Clearly, oscillatory solutions cannot occur for $\omega^2<K$. If $\omega^2=K$, then we have only one root, $r=(K-1)/\zeta_1\sqrt{K}$. For $|K-\omega^2|\ll 1$, the two roots of the above quadratic equation are well approximated by

$$r_1=\frac{K-1}{\zeta_1\sqrt{K}}+\mathcal{O}(|K-\omega^2|) \quad \text{and} \quad r_2=\frac{\zeta_1\sqrt{K}}{K-\omega^2}+\mathcal{O}(1). \tag{9}$$

Note that for $|K-\omega^2|\ll 1$ and for any fixed non-zero ϕ, depending on whether K is greater/less than ω^2, $e^{r_2\phi}$ will be *exponentially* large/small. That is, as $|r_2|\to\infty$, for any fixed $\phi>0$ and any integer $n>0$, $e^{|r_2|\phi}\gg|r_2|^n$ (see also, e.g., reference [27]).

5.2. BOUNDARY CONDITIONS

Given equation (6), along with appropriate boundary conditions, the solution $u(\phi)$ can be obtained numerically. The sole aim of this section is to establish the required boundary conditions.

As mentioned earlier, the exact extent of the contact region is unknown. Let the free (non-contact) region be between two points ϕ_A and ϕ_B, with $0<\phi_A<\phi_B<2\pi$ (see Figure 10). Contact is assumed to occur at all points on the tire between ϕ_B and ϕ_A.

The general solution in the free (non-contact) region is given by equation (6). To obtain a steady solution, we need to find the contact endpoint $\phi_{A,B}$ as well as the unknown coefficients $C_{1,2}$. Using the condition of contact at each endpoint, we obtain two equations,

$$\sec\phi_{A,B}-1=\frac{\omega^2}{1-\omega^2}+C_1 e^{r_1\phi_{A,B}}+C_2 e^{r_2\phi_{A,B}}. \tag{10}$$

If there is no concentrated force at either edge of the contact region, then the slope u_ϕ is continuous at each edge. This gives

$$\sec\phi_{A,B}\tan\phi_{A,B}=r_1C_1e^{r_1\phi_{A,B}}+r_2C_2e^{r_2\phi_{A,B}}. \tag{11}$$

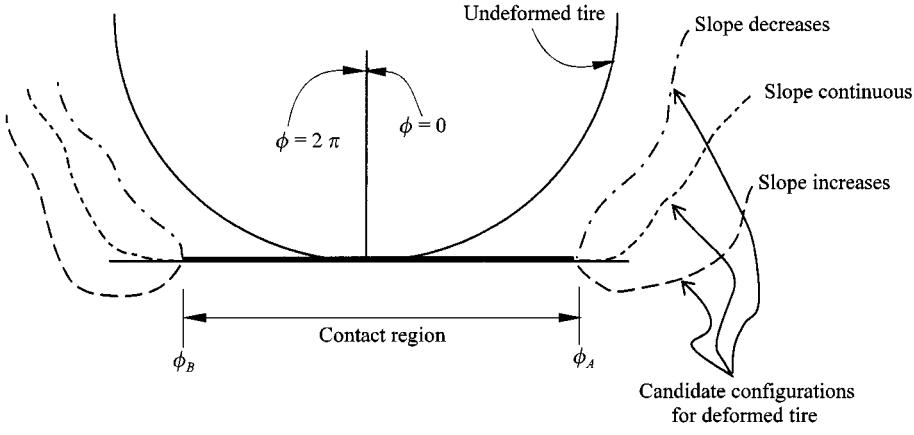

Figure 11. The geometry of solutions with and without slope discontinuities at endpoints.

On the other hand, if there is a concentrated force at one edge of the contact region, then the slope is not continuous at that edge, we cannot use equation (11) for that edge, and a different boundary condition is needed.

We now consider these two cases separately. As we show, they occur below and above critical speed, respectively.

5.2.1. *Below critical speed*

For $\omega^2 < K$, we can show that there cannot be a concentrated force at either endpoint, ϕ_A or ϕ_B. This is because $P(\phi)$ is restricted to be non-negative; hence, a concentrated force would produce a discontinuity in u_ϕ with the slope *increasing*, i.e., $u_\phi^+ > u_\phi^-$ (as seen by integrating equation (5)). A look at the contact geometry, as shown in Figure 11, shows that such behavior is not allowed at *either* endpoint, ϕ_A or ϕ_B, since it would imply interpenetration between the tire and ground. Thus, for $\omega^2 < K$, there are no concentrated forces at either endpoint, and the four conditions (equations (10) and (11)) give the four unknown quantities $C_{1,2}$ and $\phi_{A,B}$, which determine the solution.

In reference [26], the same boundary conditions were initially presented as are used here. Subsequently, an approximation was made using an extra symmetry assumption, which simplified the numerical solution procedure. We avoid that approximation here.

5.2.2. *Above critical speed*

For $\omega^2 > K$, a concentrated force at either endpoint, ϕ_A or ϕ_B, would produce a discontinuity in u_ϕ with the slope *decreasing*, i.e., $u_\phi^+ < u_\phi^-$ (as seen by integrating equation (5)). A look at the contact geometry, as shown in Figure 11, shows that such behavior is not precluded at *either* endpoint, ϕ_A or ϕ_B, since there would be no interpenetration between the tire and ground. Thus, the possibility of concentrated contact forces at either endpoint cannot be ruled out. The boundary conditions

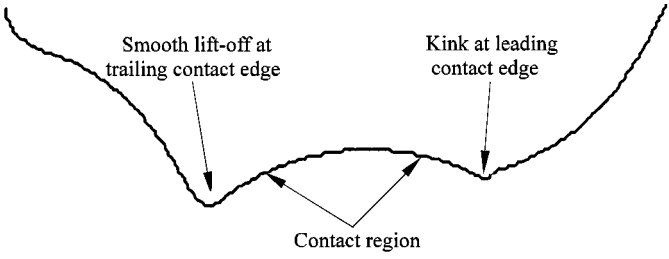

Figure 12. Lower portion of tire profile from the last shape of Figure 3, at 67 Hz. The tire is rotating clockwise.

need to be re-examined for this case, since the slope conditions of equation (11) may no longer apply.

As shown in Appendix A.1, slightly above critical speed, there appears a concentrated contact force at the *leading* edge of contact, whereas, at the *trailing* edge of contact, the distributed contact force P decreases to zero as the tire speed approaches the critical speed from below. Thus, beyond the critical speed, it is reasonable to adopt the new boundary condition of $P = 0$ at the trailing contact edge ϕ_A, and to drop the slope-continuity condition of equation (11) at the leading contact edge ϕ_B.

Thus, for zero shear damping and above the critical speed, we use the boundary conditions

$$u(\phi_{A,B}) = \sec\,\phi_{A,B} - 1,\ u_\phi(\phi_A) = \sec\phi_A \tan\,\phi_A \text{ and}$$

$$u_{\phi\phi}(\phi_A) = \sec\,\phi_A \tan^2\phi_A + \sec^3\phi_A, \tag{12}$$

where u is given by equation (6). Equation (12) may be solved numerically to obtain the four unknown quantities $C_{1,2}$ and $\phi_{A,B}$, which determines the solution.

The $P = 0$ condition (or curvature continuity) at the trailing contact edge is consistent with our experimental observations. See, for example, Figure 12, which shows an enlargement of the lower portion of the last tire profile from Figure 3. Here, the tire is rotating at 67 Hz, which is significantly above the critical speed. The leading contact edge is relatively much more sharply defined than the trailing contact edge. The relatively smooth transition from contact to non-contact at the trailing edge is consistent with the $P = 0$ or curvature continuity condition.

Furthermore, as shown in Appendix A.2, the boundary conditions adopted for zero shear damping, both below and above critical speed, may also be derived by considering the limit of small shear damping (we consider non-zero shear damping in Section 6).

Finally, as an aid to intuition, a simple physical model demonstrating this boundary condition is discussed in Appendix A.3.

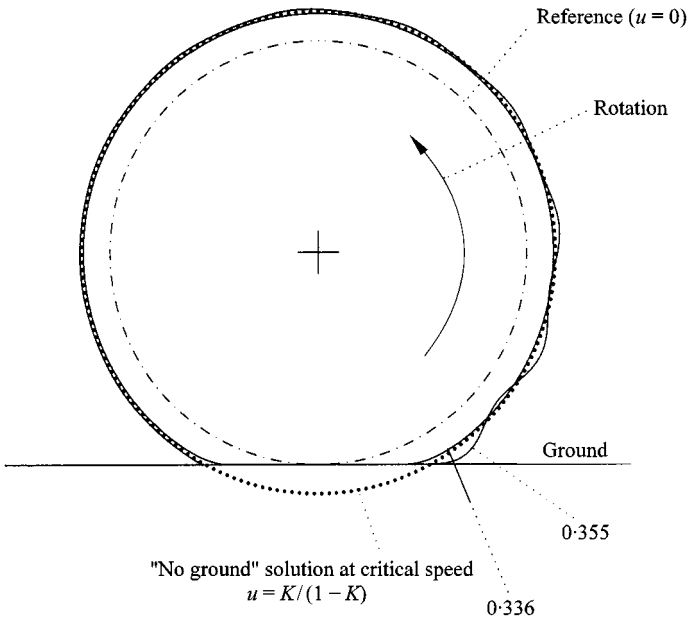

Figure 13. Solutions near critical speed $\omega^2 = K$; here $K = 0{\cdot}12$, $\zeta_1 = 0{\cdot}03$, ω as labelled ($\omega_c = \sqrt{0{\cdot}12} \approx 0{\cdot}346$).

5.3. STANDING WAVE SOLUTIONS

Standing wave solutions exist if and only if the roots of the characteristic equation are complex. For such solutions, we require that the discriminant (equation (8)) be negative i.e.,

$$\zeta_1^2 \omega^2 + 4(K - \omega^2)(1 - \omega^2) < 0.$$

For $K < \omega^2 < 1$, we find that the discriminant can be negative if the damping ζ_1 is not too large. In addition, for sufficiently small damping, equation (8) shows that the imaginary parts of $r_{1,2}$ can be very large for ω^2 very slightly larger than K.

Note that complex roots $r_{1,2}$ will necessarily have negative real parts. Thus, standing wave solutions will have amplitudes which decrease with distance from the trailing edge of the contact region. This feature will typically be retained for other contact geometries (such as, for example, a rotating tire in contact with the surface of a counter-rotating rigid drum of finite radius). The flatness, or otherwise, of the ground does not affect the roots of the characteristic equation, though it does affect the locations of the boundary points as well as the values of the coefficients $C_{1,2}$.

Some numerically obtained results for the case $K = 0{\cdot}12$, $\zeta_1 = 0{\cdot}03$ are shown in Figure 13. The numerical solutions were obtained using the Newton–Raphson technique with numerically estimated Jacobians, implemented in MATLAB. For $K = 0{\cdot}12$, the critical speed $\omega_c = \sqrt{0{\cdot}12} \approx 0.346$. As seen in the figure, just under

the critical speed ($\omega = 0{\cdot}336$), the solution is very close to the steady critical speed solution $u = \omega_c^2/(1-\omega_c^2) = K/(1-K) = 0{\cdot}136$ for the case of no contact, except for points in or close to the contact region. Just above the critical speed ($\omega = 0{\cdot}355$), there are standing waves that are qualitatively similar to those observed experimentally.

6. SOLUTIONS FOR NON-ZERO SHEAR DAMPING

It was shown in Section 5 that the rotating tire model, as given by equation (1), predicts standing wave solutions beyond the critical speed if the shear damping term is taken to be zero. In this section, we consider solutions for non-zero shear damping. Not surprisingly perhaps, we find that a small amount of shear damping does not change the basic nature of the standing wave solutions, though shear damping does have a stronger attenuating effect than radial damping.

6.1. CHARACTERISTIC EQUATION

The radial displacement u satisfies equation (3), with the distributed contact force $P(\phi) = 0$ in the free (non-contact) region. The associated characteristics equation is

$$\zeta_2 \omega r^3 + (K - \omega^2) r^2 - \zeta_1 \omega r - (1 - \omega^2) = 0. \tag{13}$$

In order to have standing wave solutions at some rotation speed ω, we require two of the roots of the characteristic equation to be complex. For the standing waves to have decaying amplitude with increasing distance from the trailing edge of the contact region, the two complex roots must have *negative* real parts. As discussed earlier, while the contact or boundary conditions determine the location and extent of the contact region, and can influence the amplitude of the standing wave, the wavelength and spatial attenuation rate are determined solely by the roots of the characteristic equation.

We assume light damping (ζ_1 and ζ_2 comparable, and very small compared to 1). Not too close to the critical speed $\omega_c = \sqrt{K}$, equation (13) is a singularly perturbed quadratic equation in r. Thus, two of its roots will be the roots of that original quadratic equation perturbed slightly by $\mathcal{O}(\zeta_2)$ amounts, while the (new) third root will be $\mathcal{O}(1/\zeta_2)$ or large in magnitude (see, e.g., reference [27]).

By a straightforward calculation (see, e.g., reference [27]), we find that not too close to the critical speed, the roots of the characteristic equation are

$$r_{1,2} = \pm \sqrt{\frac{1-\omega^2}{K-\omega^2}} + \mathcal{O}(\zeta) \quad \text{and} \quad r_3 = -\frac{K-\omega^2}{\zeta_2 \omega} + \mathcal{O}(\zeta), \tag{14}$$

where the small correction term of $\mathcal{O}(\zeta)$ represents terms of order ζ_1 and/or ζ_2.

Below the critical speed, all three roots are real. The introduction of the small shear damping term does not change the solution much except for the addition of

a real root r_3 of large magnitude. Oscillatory solutions, or standing waves, do not occur.

On the other hand, the leading-order expressions for $r_{1,2}$ are purely imaginary *above* critical speed. This shows that standing waves persist in the presence of small damping. In order to see how they are spatially attenuated due to damping, we need a higher order approximation. At the next order of approximation, we find

$$r_{1,2} = -\frac{\omega}{2(\omega^2 - K)}\left(\zeta_1 + \frac{1-\omega^2}{\omega^2 - K}\,\zeta_2\right) \pm \mathrm{i}\,\sqrt{\frac{1-\omega^2}{\omega^2 - K}} + \mathcal{O}(\zeta^2), \tag{15}$$

showing that standing waves decay in the same direction as for the case of zero shear damping. It is interesting to note that the effect of the shear damping ζ_2 will be stronger than that due to the radial damping ζ_1 since $(1-\omega^2)/(\omega^2 - K)$ is large in the speed range of interest (e.g., for $K = 0{\cdot}12$, even for $\omega = 1{\cdot}3\omega_c$ or 30% above critical speed, $(1-\omega^2)/(\omega^2 - K) \approx 9.6$).

Finally, note in equation (14) that the third root r_3 is clearly large and positive sufficiently far above the critical speed, and large and negative sufficiently far below critical speed.

6.2. BOUNDARY CONDITIONS

Solutions to equation (3) in the non-contact region are of the form

$$u(\phi) = \frac{\omega^2}{1-\omega^2} + C_1\,\mathrm{e}^{r_1\phi} + C_2\mathrm{e}^{r_2\phi} + C_3\mathrm{e}^{r_3\phi}, \tag{16}$$

where $r_{1,2,3}$ satisfy the characteristic equation, equation (13). As before, let the endpoints of the contact region be ϕ_A and ϕ_B, with $0 < \phi_A < \phi_B < 2\pi$.

For non-zero shear damping ζ_2 and rotation speed ω, it can be seen by integrating equation (3) that a concentrated contact force at an endpoint of the contact region produces a discontinuity in $u_{\phi\phi}$. In particular, $u_{\phi\phi}$ increases by an amount $\mathcal{O}(\zeta_2\omega)$. The geometry of the contact region is such that if $u_{\phi\phi}$ changes discontinuously at an endpoint of the contact region, then it can only decrease at the left endpoint ϕ_A and increase at the right endpoint ϕ_B (otherwise, interpenetration would occur between tire and ground). This means that a concentrated contact force, if any, must exist at ϕ_B and not ϕ_A, and that $u_{\phi\phi}$ is continuous at ϕ_A.

There are five unknowns, the endpoints $\phi_{A,B}$ and the coefficients $C_{1,2,3}$. To determine these, we have two conditions of contact or continuity of displacement u, two conditions on continuity of slope u_ϕ, and one condition on continuity of curvature $u_{\phi\phi}$ at the left endpoint ϕ_A.

$$u(\phi_{A,B}) = \sec\phi_{A,B} - 1, \quad u_\phi(\phi_{A,B}) = \sec\phi_{A,B}\tan\phi_{A,B}$$

and

$$u_{\phi\phi}(\phi_A) = \sec\phi_A\tan^2\phi_A + \sec^3\phi_A, \tag{17}$$

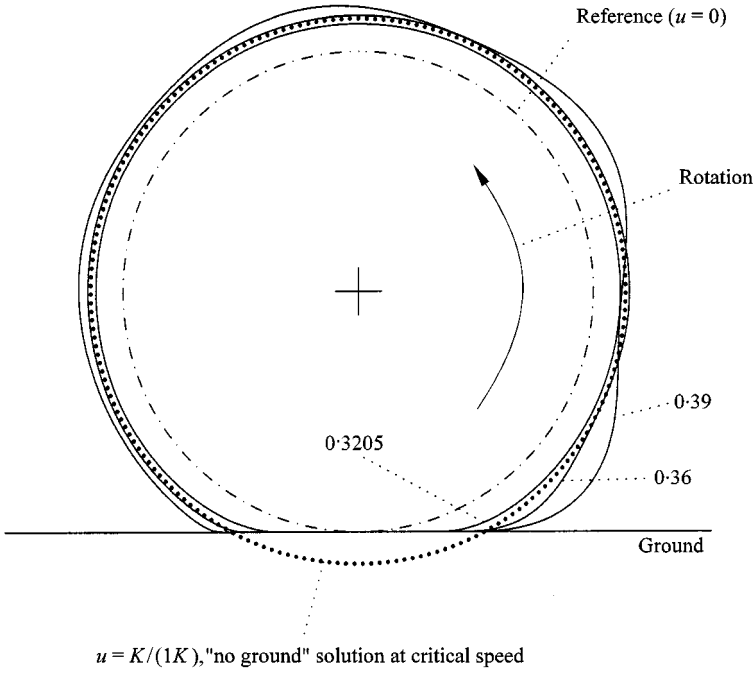

Figure 14. Standing wave solutions with nonzero shear damping: $K = 0{\cdot}12$, $\zeta_1 = 0{\cdot}03$, $\zeta_2 = 0{\cdot}003$, ω as labelled.

where u is given by equation (16). Solving these equations numerically, we can simultaneously determine the extent of the contact region as well as displacements in the non-contact region. As before, the numerical solutions were obtained using the Newton–Raphson technique with numerically estimated Jacobians, implemented in MATLAB.

6.3. STANDING WAVE SOLUTIONS

Numerically obtained steady solutions for rotation speed ω close to the critical speed $\omega_c = \sqrt{K}$ are shown in Figure 14. As discussed in the previous section, the damping effect of ζ_2 is stronger than that of ζ_1, especially near the critical speed. Figures 13 and 14 show that a rather small value of ζ_2 (one-tenth of ζ_1) has a marked effect on both the amplitude as well as attenuation rate of standing wave solutions. Thus, in an experimental context, standing waves will first be observed at a speed *larger* than the theoretically determined value of ω_c.

7. THE INFLUENCE OF NON-ZERO FLEXURAL RIGIDITY

The model of the balloon tire studied in previous sections allows standing wave solutions that decay in amplitude with increasing distance from the trailing edge of the contact region, much as observed in experiments. However, as mentioned in the

introduction, the experimental system near the critical speed also develops small, sharply decaying ripples near the leading edge of the contact region. In this section, we describe how such an effect can be due to a small "beam-like" or flexural rigidity term.

We assume that the non-dimensional flexural rigidity is much smaller than the damping effects. Guided by previous results, we further assume that the shear damping is much smaller than the radial damping which in turn is small compared to 1. Accordingly, we modify the non-dimensional equation (2) to

$$u_{\tau\tau} - \omega^2 (1 + u) = -u - \varepsilon\eta_1 u_\tau + K u_{\theta\theta} + \varepsilon^2 \eta_2 u_{\theta\theta\tau} - \varepsilon^3 u_{\phi\phi\phi\phi} - P(\theta, \tau), \quad (18)$$

where the radial damping term $\zeta_1 = \varepsilon\eta_1$, the shear damping term $\zeta_2 = \varepsilon^2\eta_2$, and the non-dimensional flexural rigidity is ε^3, for some suitable $0 < \varepsilon \ll 1$. As before, we write the ordinary differential equation describing steady standing wave solutions in lab-fixed co-ordinates,

$$-\varepsilon^2 u_{\phi\phi\phi\phi} + \varepsilon^2 \eta_2 \omega u_{\phi\phi\phi} + (K - \omega^2) u_{\phi\phi} - \varepsilon\eta_1 \omega u_\phi - (1 - \omega^2)u + \omega^2 = P(\phi). \quad (19)$$

The characteristic equation associated with equation (19) is

$$-\varepsilon^3 r^4 + \varepsilon^2 \eta_2 \omega r^3 + (K - \omega^2) r^2 - \varepsilon\eta_1 \omega r - (1 - \omega^2) = 0. \quad (20)$$

We do not conduct a complete analysis of equation (20). Our main interest here is to discuss the effect of the small flexural rigidity term on the nature of possible standing wave solutions. In particular, to illustrate how ripples near the contact edge arise, we examine the simplest case when ω is not too close to the critical speed $\sqrt{K}$ (i.e., where $K - \omega^2$ can be treated as $\mathcal{O}(1)$ compared to ε).

Equation (20) has four roots, two of which are slightly (i.e., $\mathcal{O}(\varepsilon^2)$) perturbed versions of the already familiar roots of the quadratic equation (see equation (7))

$$(K - \omega^2) r^2 - \varepsilon\eta_1 \omega r - (1 - \omega^2) = (K - \omega^2) r^2 - \zeta_1 \omega r - (1 - \omega^2) = 0.$$

The other two roots are "large", and are approximated as follows. First, we assume that the roots are of the form $r = \lambda/\varepsilon^s$, where $\lambda = \mathcal{O}(1)$ and $s > 0$ is to be determined. Substituting into equation (20), we obtain

$$-\varepsilon^{3-4s}\lambda^4 + \varepsilon^{2-3s}\eta_2 \omega \lambda^3 + \varepsilon^{-2s}(K - \omega^2)\lambda^2 - \varepsilon^{1-s}\eta_1 \omega \lambda - (1 - \omega^2) = 0.$$

To determine s, we note that no single term in the equation can be asymptotically bigger than all the others. Balance between the two largest terms occurs for $s = 3/2$, and we obtain

$$-\varepsilon^{-3}\lambda^4 + \varepsilon^{-5/2}\eta_2 \omega \lambda^3 + \varepsilon^{-3}(K - \omega^2)\lambda^2 - \varepsilon^{-1/2}\eta_1 \omega \lambda - (1 - \omega^2) = 0.$$

Multiplying through by ε^3, we obtain

$$-\lambda^4 + \varepsilon^{1/2}\eta_2 \omega \lambda^3 + (K - \omega^2)\lambda^2 - \varepsilon^{5/2}\eta_1 \omega \lambda - \varepsilon^3 (1 - \omega^2) = 0.$$

which we write as

$$-\lambda^4 + \varepsilon^{1/2}\eta_2\omega\lambda^3 + (K - \omega^2)\lambda^2 + \mathcal{O}(\varepsilon^{5/2}) = 0.$$

Temporarily ignoring the small $\mathcal{O}(\varepsilon^{5/2})$ term, we note that the above fourth order equation has two roots equal to zero; these are merely the $\mathcal{O}(1)$ roots disguised by the singular scaling. Solving a quadratic to obtain the other two roots and returning to the old variable r, we obtain

$$r_{3,4} = \frac{\eta_2\omega}{2\varepsilon} \pm \sqrt{\frac{\eta_2^2\omega^2}{4\varepsilon^2} - \frac{\omega^2 - K}{\varepsilon^3}} + \mathcal{O}(\varepsilon),$$

which in terms of system parameters is

$$r_{3,4} = \frac{\zeta_2\omega}{2\varepsilon^3} \pm \sqrt{\frac{\zeta_2^2\omega^2}{4\varepsilon^6} - \frac{\omega^2 - K}{\varepsilon^3}} + \mathcal{O}(\varepsilon). \tag{21}$$

It is worthwhile to briefly examine equation (21) using a numerical example. We pick $K = 0{\cdot}12$, $\zeta_1 = 0{\cdot}03$, $\zeta_2 = 2{\cdot}0 \times 10^{-4}$, and $\varepsilon^3 = 1{\cdot}0 \times 10^{-5}$. Note that $\varepsilon \approx 2{\cdot}15 \times 10^{-2}$. Now, picking $\omega = 0{\cdot}6$ for purposes of illustration, we have $K - \omega^2 \approx -0{\cdot}240$, which is an order of magnitude larger than ε, consistent with the foregoing analysis. For these values, the numerically evaluated "large" roots of equation (20) are $6{\cdot}0382 \pm \mathrm{i}\,154{\cdot}7960$, while the roots predicted by equation (21) are $6{\cdot}000 \pm \mathrm{i}\,154.8031$, with an error magnitude of $3{\cdot}88 \times 10^{-2}$ which is comparable to ε as expected. As another example, for $\omega = 0{\cdot}37$, closer to the critical speed, we have $K - \omega^2 \approx -1{\cdot}69 \times 10^{-2}$, which is comparable to ε. In this case, the above asymptotic error estimate of $\mathcal{O}(\varepsilon)$ is not expected to be good. As expected, in this case, the numerically obtained roots are $4{\cdot}1703 \pm \mathrm{i}\,40{\cdot}3485$, while the roots predicted by equation (21) are $3{\cdot}7000 + \mathrm{i}\,40{\cdot}9428$, with an error magnitude of $0{\cdot}758$, which is an order of magnitude larger than ε. However, a reasonable approximation is still obtained in this case. The preceding examples verify that, sufficiently far from critical speed, equation (21) gives a good approximation to the roots of the characteristic equation.

Note in equation (21) that the real parts are *positive*. Thus, beyond the critical speed, the presence of sufficiently small flexural rigidity ε^3 and shear damping $\zeta_2 = \varepsilon^2\eta_2$ (with $\eta_2 = \mathcal{O}(1)$) gives rise to two pairs of complex roots. One pair, $\mathcal{O}(1)$ in magnitude, has negative real parts and causes standing waves of wavelength $\mathcal{O}(1)$ to decay with increasing distance from the trailing edge of the contact region. The other pair, large in magnitude, has large positive real parts and causes small-wavelength standing waves (i.e., ripples) to appear over a short distance near the leading edge of the contact region, as observed qualitatively in the experiment.

We remark that in this case, the second derivative $u_{\phi\phi}$ must be continuous at both endpoints of the contact region, even if concentrated contact forces are present (which they are). This gives us the extra boundary condition needed, in addition to

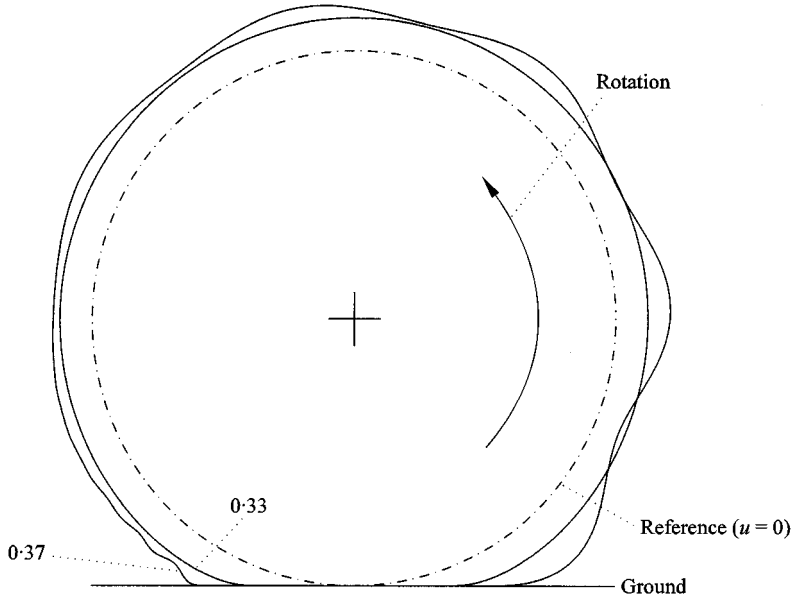

Figure 15. Standing wave solutions with non-zero flexural rigidity showing a ripple ahead of the contact patch: $K = 0{\cdot}12$, $\zeta_1 = 0{\cdot}03$, $\zeta_2 = 2 \times 10^{-4}$, $\varepsilon^3 = 1{\cdot}0 \times 10^{-5}$ ($\varepsilon \approx 2{\cdot}154 \times 10^{-2}$), ω as labelled. See text for discussion.

those for the shear damping case (equation (17)). Using these, and parameter values used in the example above, a numerical example is shown in Figure 15. The ripple near the leading edge of contact is clearly visible.

8. QUALITATIVE COMPARISON WITH EXPERIMENTS

The model presented in this paper is capable of capturing several qualitative features of the experimental system.

For small damping, the model predicts standing wave solutions beyond some transition speed just above the theoretical critical speed, $\omega_c = \sqrt{K}$. These standing waves appear behind the contact region, and decay with increasing distance from its trailing edge. The spatial attenuation rate of these waves decreases with increasing rotation speed, while the amplitude and wavelength increase. All of these features are observed in the experimental system.

With a small amount of shear damping and smaller flexural rigidity, the model also predicts sharply decaying ripples near the leading edge of the contact region. This feature is also observed in the experimental system.

We now briefly present the predicted spatial frequency and attenuation rate (log decrement in amplitude) for standing wave solutions. For simplicity, we ignore both the shear damping ζ_2 as well as the small flexural rigidity discussed in the previous section. For the model, we use $K = 0{\cdot}12$ as estimated from a static deflection test, and $\zeta_1 = 0{\cdot}03$ as before. Predicted spatial frequency and spatial

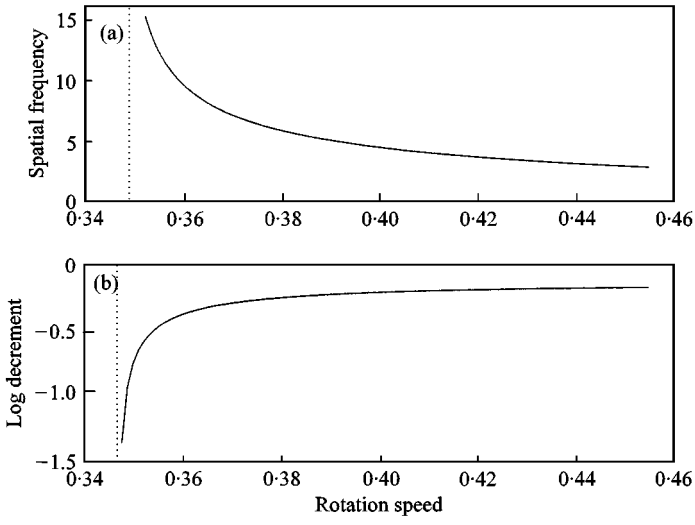

Figure 16. Predicted trends from model, for $K = 0{\cdot}12$, $\zeta_1 = 0{\cdot}03$, and no shear damping. Dotted line marks $\omega_c = \sqrt{0{\cdot}12}$: (a) Spatial frequency, (b) log decrement.

attenuation rate (log decrement between successive peaks) are plotted against ω in Figure 16. These curves are consistent with experimental observations (see Figure 6); in particular, it is seen that spatial frequency and attenuation rate both decrease monotonically with increasing rotation speed, in the range studied.

9. PHYSICAL INTERPRETATION

It is worthwhile at this point, in light of the mathematical analysis carried out in the previous sections, to address the question of the physical origin of the standing waves. For simplicity, we consider only the case of zero shear damping and flexural rigidity (i.e., Section 5).

The natural frequencies ω_n of free vibrations of the stationary tire, without damping, may easily be found as

$$\omega_n = \sqrt{1 + n^2 K} \quad \text{for } n = 1, 2, \ldots,$$

where we omit the $n = 0$ or breathing mode, which is usually perceived as being not important for standing waves (e.g., reference [14]). Using the resonance condition proposed in reference [14], we find the predicted critical speed to be

$$\min_{n = 1, 2, \ldots,} \frac{\omega_n}{n} = \sqrt{K} = \omega_c \tag{22}$$

which is correct (on interpreting the minimum as an infimum). For zero damping, the minimizing n in the resonance condition also gives the characteristic

wavelength of the standing wave. In our case, since $n = \infty$, the wavelength predicted by the resonance condition is exactly zero. For small damping, the wavelength at the onset of the standing waves is small, which qualitatively matches the prediction of the resonance condition as well.

However, though standing waves first appear at a speed near ω_c for small damping, they persist for all higher rotation frequencies. To quote reference [1], "It is not possible to drive through to a higher speed where the tire again runs smoothly (i.e., without large standing waves)." As observed in experiment and as predicted by our analysis, the size and shape of the standing wave vary monotonically with rotation speed in the range studied. Hence, in spite of the successful prediction of the critical speed by the resonance condition, for the system with damping and well above critical speed it seems inappropriate to attribute the standing waves to a *resonance* in the usual sense of the word.

Another popular interpretation of standing waves is based on the shock at the leading contact edge. However, the magnitude of the shock has no effect on the size or shape of the standing wave. By our analysis, these properties are determined solely by the lift-off conditions at the trailing contact edge along with the roots of the characteristic equation. Thus, the *shock* does not cause the standing wave, though the two appear at approximately the same speed for light radial damping.

Finally, can we think of the formation of standing waves as resulting from an *instability*? Such a view implies that the non-oscillatory steady state solution continues to exist, but becomes unstable. However, since the eigenvalues r_1 and r_2 are complex whenever standing waves exist, it is easy to see, by examination of equation (10), that the only possible co-existing non-oscillatory solution is a constant that cannot satisfy the boundary conditions. In other words, once contact-induced standing waves have appeared, a non-oscillatory solution *no longer* exists. Thus, an instability interpretation is not meaningful for this system.

We therefore conclude that the formation of standing waves in tires is not a resonance phenomenon (at least in the usual sense), is not caused by a shock (though it is accompanied by one), and cannot be interpreted as an instability. Of the three, while not completely justifiable, the resonance interpretation has some merit in that it does appear to predict the correct critical speed.

Our approach in this paper has been to simply study the boundary value problem that governs contact-induced standing waves. This approach has allowed us to obtain some simple but useful insights. Mathematically, it is clear that the standing waves are possible whenever the roots of the characteristic equation are complex. Physically, the existence of complex roots reflects the fact that the time scale of the rotation is in some sense shorter than the time scale of the transient vibrations excited by the contact forces. At speeds where standing waves are possible, the boundary conditions determine the amplitudes of these waves. In particular, for our system, the boundary conditions at the trailing contact edge have by far the greatest influence on the amplitude of the standing wave. These basic properties of the standing waves allow us to develop a technique for suppressing the standing waves, as we show next.

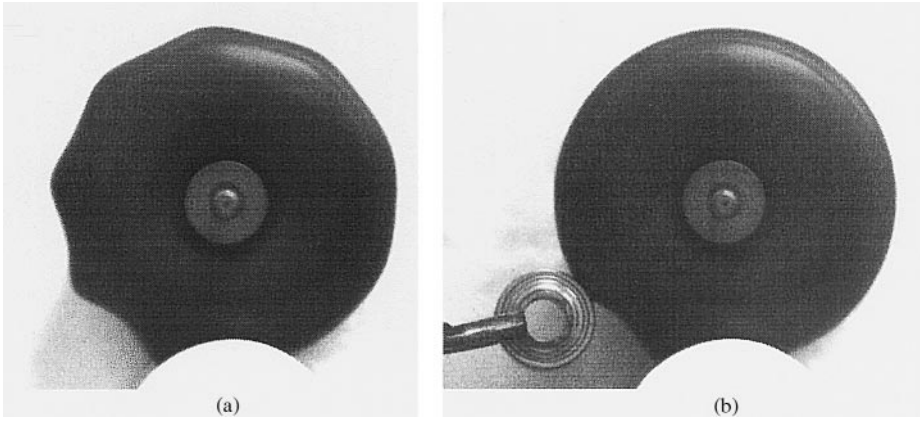

Figure 17. Active suppression of the tire standing wave is possible with a single external force, as predicted by the theory. The tire is rotating clockwise: (a) Standing wave, (b) suppressed.

10. SUPPRESSION OF THE STANDING WAVE

Our analysis predicts that the leading edge of contact does not significantly influence the size or shape of the standing wave. The standing wave can therefore be controlled by controlling the trailing edge behavior.

Based on this theoretical observation, we conducted one final, simple experiment. A tire was rotated faster than its critical speed so that it had a standing wave on it. A ball bearing was held by its inner race using a wrench, so that the outer race could spin freely. This bearing was manually brought into contact with the rotating tire at a point some small distance away from the trailing contact edge. The effect of applying an external force at this point was examined. The results are shown in Figure 17.

Figure 17(a) shows the tire with no external forces on it except from the "ground" contact, and the standing wave is seen to extend all the way around the tire. In Figure 17(b), the effect is shown of applying a force at a point close to the ground contact. The tire now has two contact regions: the old or ground contact, and the new or bearing contact.

In the region between the trailing edge of ground contact and the leading edge of bearing contact, as predicted by the theory, there is essentially no change in the behavior of the tire: Figures 17(a) and (b) appear identical in this region.

On the other hand, in the region between the trailing edge of bearing contact and the leading edge of ground contact, i.e., most of the tire as seen in Figure 17(b), the size of the standing wave is determined by the conditions at the trailing edge of bearing contact. As seen in the figure, appropriate positioning of the bearing can totally remove the standing wave behind the bearing contact.

This last experiment suggests a possible means for active suppression of standing waves in such rotating systems. This approach should also work in the case of tires with substantial amounts of flexural rigidity, although in such cases one might have to apply two external forces, one on each side of the contact region.

11. CONCLUSIONS

A small-scale tire test rig has been described which is capable of driving small ballon tires past the speed at which standing waves first appear. Using video image processing, we have obtained complete quantitative data sets for the standing waves for various initial tire pressures and for a range of tire angular velocities. Beyond just detecting the critical speed, the change in the spatial structure of the standing waves with increasing tire rotational speed can be visualized in detail: the results are seen to be in good qualitative agreement with other numerical work, as well with our own simple model presented and analyzed in detail in this same paper.

The model presented here is amenable to analytical treatment, yet incorporates geometrically realistic contact conditions and captures the qualitative behavior of the experimental system studied in the laboratory.

A well-defined critical speed for the tire has been identified in terms of model parameters. Standing waves appear behind the trailing edge of contact when the tire rotates steadily at speeds beyond this critical speed, as observed experimentally. These standing waves have been examined as solutions to a non-linear boundary value problem. Questions regarding boundary conditions, for the case of zero and non-zero shear damping, have been addressed in detail.

For the case of zero shear damping it was found that beyond critical speed, a concentrated contact force appears at the leading edge of the contact region. The appearance of this concentrated contact force corresponds to a shock, taken here to mean a discontinuity in u_ϕ. With non-zero shear damping, it was found that a small concentrated contact force is present at the leading edge of contact even for rotation speeds below the critical speed, and the shock (discontinuity in u_ϕ) is not seen. Introduction of a small amount of flexural rigidity was found to cause small ripples near the leading edge of contact, much as observed experimentally.

Theoretically predicted qualitative trends in standing wave wavelength and spatial attenuation rate, as a function of rotation speed, compared favourably with experimental measurements.

The analysis in this paper leads to the conclusion that above critical speed the trailing edge boundary conditions essentially control the amplitude and wavelength of the standing waves. Based on this observation, a means for active suppression of standing waves in such rotating system was demonstrated experimentally.

ACKNOWLEDGMENTS

This work was supported in part by Wright Laboratories, WL/FIVMA. In particular, we wish to thank Arnold Meyer and the late Mangal Chawla for their support in the early stages of this project.

REFERENCES

1. W. F. Ames 1970 *Textile Research Journal* **20**, 498–503. Waves in tires.
2. S. K. Clark (editor) 1981 *Mechanics of Pneumatic Tires. DOT* HS 805952, U.S. Department of Transportation National Highway Safety Administration.

3. D. N. Dodge 1965 *SAE Paper* 650491, *Midyear Meeting*, *Chicago*, IL. The dynamic stiffness of a pneumatic tire model.
4. S. K. Clark 1965 *SAE Paper* 650493, *Midyear Meeting*, *Chicago*, *IL*. The rolling tire under load.
5. J. T. Tielking 1965 *SAE Paper* 6504925, *Midyear Meeting*, *Chicago*, *IL*. Plane vibration characteristics of a pneumatic tire model.
6. G. R. Potts, C. A. Bell, L. T. Charek and T. K. Roy 1977 *Tire Science and Technology*, *TSTCA* **5**, 202–225. Tire vibrations.
7. W. B. Bickford and E. S. Reddy 1985 *Journal of Sound and Vibration* **101**, 13–22. On the in-plane vibrations of rotating rings.
8. S. C. Huang and W. Soedel 1987 *Journal of Sound and Vibration* **115**, 253–274. Effects of Coriolis acceleration on the free and forced in-lane vibration of rotating rings on elastic foundation.
9. S. C. Huang and W. Soedel 1987 *Journal of Sound and Vibration* **118**, 253–270. Response of rotating rings to harmonic and periodic loading and comparison with the inverted problem.
10. S. C. Huang 1992 *International Journal of Vehicle Design* **13**, 78–95. The vibration of rolling tyres in ground contact.
11. S. C. Huang and C. K. Su 1992 *Vehicle System Dynamics* **21**, 247–267. In-plane dynamics of tires on the road based on an experimentally verified rolling ring model.
12. N. J. Lindlsey and J. P. Cusumano 1993 *SAE Paper* 932580, *Aerotech* '93, *Costa Mesa*, *CA*. Critical speed analysis of a non-linear strain ring dynamical model for aircraft tires.
13. E. Vinesse and H. Nicollet 1988 *Journal of Sound and Vibration* **126**, 85–96. Surface waves on the rotating type: an application of functional analysis.
14. W. Soedel 1975 *Journal of Sound and Vibration* **41**, 233–246. On the dynamic response of rolling tires according to thin shell approximations.
15. J. Padovan 1976 *Tire Science and Technology*, *TSTCA* **4**, 233–246. On viscoelasticity and standing waves in tires.
16. J. Padovan 1977 *Tire Science and Technology*, *TSTCA* **5**, 83–101. On standing waves in tires.
17. L. E. Kung, W. Soedel and T. Y. Yang 1986 *Journal of Sound and Vibration* **107**, 181–194. Free vibration of a pneumatic tire-wheel unit using a ring on an elastic foundation and a finite element model.
18. R. Kennedy and J. Padovan 1987 *Tire Science and Technology*, *TSTCA* **15**, 243–260. Finite element analysis of a steady-state rotating tire subjected to a point load or ground contact.
19. J. H. Champion and P. M. Wagner 1988 *AFWAL-TR*-88-3006, *U.S. Airforce*. A critical speed study for aircraft bias ply tires.
20. J. Padovan, A. Kasempour, F. Tabaddor and B. Brockman 1989 *SAE Paper* 892349. Evaluation of critical speeds in high speed aircraft tires.
21. M. Hirano and T. Akasaka 1976 *Tire Science and Technology*, *TSTCA* **4,** 86–114. Natural frequencies of the bias tire.
22. L. E. Kung 1990 *SAE Paper* 900759. Radial vibrations of pneumatic radial tires.
23. R. W. Scavuzzo, T. R. Richards and L. T. Charek 1993 *Tire Science and Technology*, *TSTCA* **21**, 23–39. Tire vibration modes and effects on vehicle ride quality.
24. P. M. Wagner 1989 *WRDC-TM*-89-194-*FIVMA*, *U.S. Air Force*. Initial critical speed laboratory tests of three aircraft bias ply tires.
25. J. Medzorian 1991 *Internal Report*, *Wright Laboratories*/*FIVMA*, *U.S. Air Force*. Prediction of aircraft tire critical speed by natural frequency extraction.
26. D. S. Stutts and W. Soedel 1992 *Journal of Sound and Vibration* **155**, 153–164. A simplified dynamic model of the effect of internal damping on the rolling resistance in pneumatic tires.
27. E. J. Hinch 1991 *Perturbation Methods*. Cambridge: Cambridge University Press.

APPENDIX A: BOUNDARY CONDITIONS FOR ZERO SHEAR DAMPING

A.1. BEHAVIOR CLOSE TO CRITICAL SPEED

We will now show that slightly above critical speed (for $|K - \omega^2| \ll 1$), a concentrated force appears at the leading edge of contact, i.e., at ϕ_B. We will also show that exactly at critical speed, the magnitude of the distributed contact force P drops to zero at the trailing contact edge ϕ_A. Since P cannot be negative, this leads to the hypothesis that $P(\phi_A) = 0$ above critical speed.

Let us first consider the situation slightly *below* critical speed. As ω^2 approaches K from below, equations (6) and (9) show that the solution of u contains two exponential parts, one (due to r_1) which decreases at a finite or bounded rate, and another (due to $r_2 \gg 1$) which increases very rapidly with ϕ due to equation (9). This implies the existence of a boundary layer at the leading edge of the contact patch, i.e., at ϕ_B (see Figure 18). For a detailed discussion of such singularly perturbed equations, see e.g., reference [27]. For completeness, a brief discussion of the main ideas are presented below, in the context of the problem at hand.

Consider the second exponential term in the solution, given by $C_2 \, e^{r_2 \phi}$, and note that just below critical speed $r_2 \gg 1$. It follows that near the right boundary point ϕ_B, where ϕ is greatest, the magnitude of this term is *much* larger than at points far removed from this boundary point. In fact, outside a narrow boundary layer near ϕ_B, of width $\mathcal{O}(1/r_2)$, this term has exponentially small magnitude and may be ignored. Thus, far from ϕ_B and in particular close to ϕ_A, we may drop the second term and simply write

$$u = \frac{\omega^2}{1 - \omega^2} + C_1 \, e^{r_1 \phi} \tag{A.1}$$

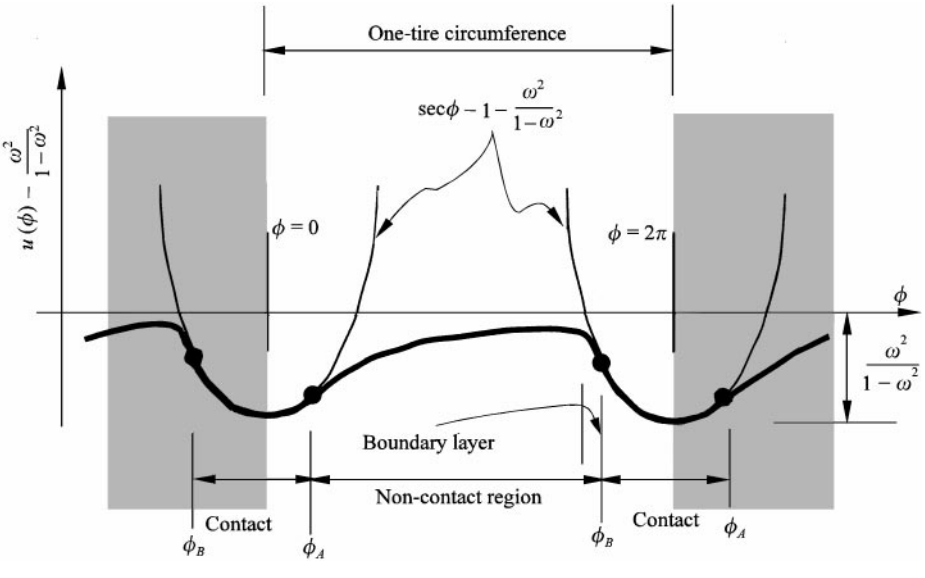

Figure 18. Just below the critical speed $\omega_c = \sqrt{K}$, the solution has a boundary layer near the right endpoint ϕ_B of the domain, i.e., the leading edge of the contact region (for the case of zero shear damping, $\zeta_1 > 0$, and $\omega^2 < K$).

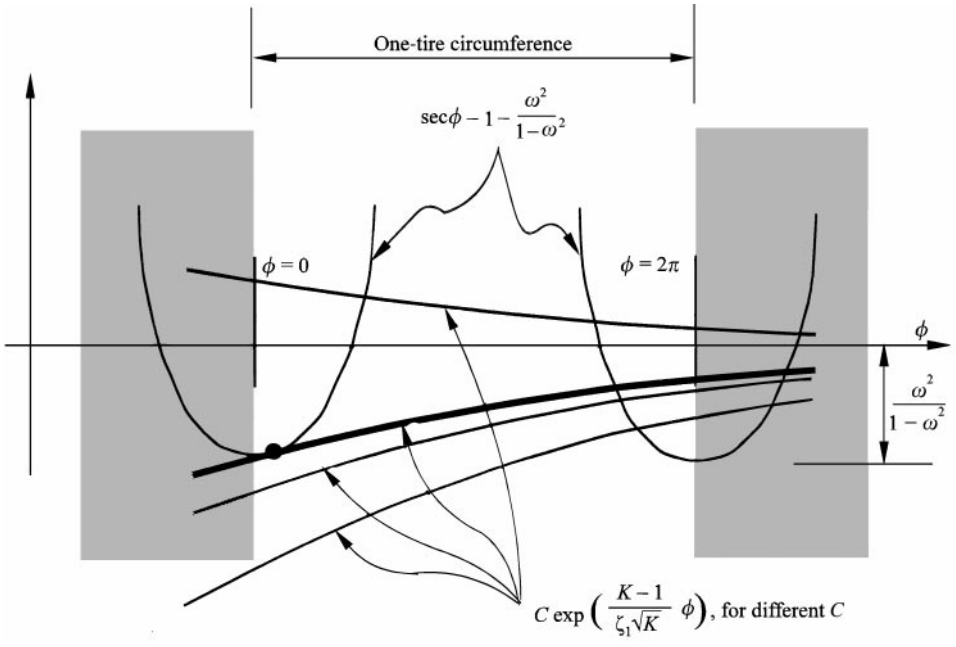

Figure 19. The curves $u = \sec\phi - 1 - (\omega^2/(1-\omega^2))$ and $C_1 e^{r_1\phi}$ are tangential for a unique pair of (C_1, ϕ_A), for $\phi_A \in (0, 2\pi)$.

(in the singular perturbations literature, equation (A.1) would be referred to as the *outer* solution).

At endpoint ϕ_A, and infinitesimally below critical speed, equation (10) may therefore be written

$$\sec\phi_A - 1 - \frac{\omega^2}{1-\omega^2} = C_1 e^{r_1\phi_A},$$

while equation (11) may be written as

$$\sec\phi_A \tan\phi_A = r_1 C_1 e^{r_1\phi_A}.$$

The last two equations can now be solved for ϕ_A and C_1, *independently* and without knowledge of ϕ_B and C_2. In particular, we can make a simple geometric interpretation of these last two equations: the graph of $C_1 e^{r_1\phi}$ makes *grazing* contact with, or is tangent to, the graph of $\sec\phi - 1 - (\omega^2/(1-\omega^2))$ at the point ϕ_A. This geometrical interpretation is shown in Figure 19.

Now consider the situation slightly *above* critical speed. In this case, r_2 is large and negative, while r_1 is essentially unchanged. Thus, the second exponential term in u, given by $C_2 e^{r_2\phi}$, now decays very rapdily, and may be neglected outside a narrow boundary layer near ϕ_A of width $\mathcal{O}(1/|r_2|)$. Far from the boundary layer, and in particular close to ϕ_B, the solution is again given by

$$u = \frac{\omega^2}{1-\omega^2} + C_1 e^{r_1\phi}.$$

Now we are in a position to prove our claim that slightly above critical speed there must be a concentrated contact force at ϕ_B. We prove this by contradiction. Accordingly, we assume that there is no concentrated contact force at ϕ_B. Similar to the below critical speed case, we must now have the conditions

$$\sec\phi_B - 1 - \frac{\omega^2}{1-\omega^2} = C_1 e^{r_1\phi_B}$$

and

$$\sec\phi_B \tan\phi_B = r_1 C_1 e^{r_1\phi_B}.$$

Geometrically, as before, this means that the graph of $C_1 e^{r_1\phi}$ must be tangent to the graph of $\sec\phi - 1 - (\omega^2/(1-\omega^2))$ at the point ϕ_B. However, as is clear from Figure 19, such tangency *cannot* occur in the interval $3\pi/2 < \phi < 2\pi$ for *any* C_1. In other words, we have a contradiction, and conclude that there *must* be a concentrated force at the leading contact edge ϕ_B, at speeds slightly above critical speed.

Since the magnitude of the concentrated force is unknown, the solution is indeterminate at this point, and we need to impose an additional, suitable condition in order to obtain a physically meaningful solution. Such an additional condition can be found from the following observation.

As mentioned in Section 4, the magnitude of the distributed contact force P need not be zero at the endpoints of the contact region. However, we now observe that the distributed contact force P drops to zero exactly at the critical speed. As discussed above, as the rotation speed approaches the critical speed from below, i.e., as $\omega \uparrow \sqrt{K}$, there is no boundary layer near ϕ_A. Consequently, the non-contacting solution near ϕ_A has a bounded second derivatives as $\omega \uparrow \sqrt{K}$. Obviously, for $\phi_A < \pi/2$ (a finite contact region), the second derivative of u in the contact region is determined solely by contact geometry and is also bounded near ϕ_A. Both (contact region and non-contact region) second derivatives being bounded as the critical speed is approached, we can take the limit in each case and compare the two at ϕ_A.

Equation (5) becomes

$$-\zeta_1 \omega u_\phi(\phi_A) - (1-\omega^2)\, u(\phi_A) + \omega^2 = P(\phi_A)$$

in the contact region and

$$-\zeta_1 \omega u_\phi(\phi_A) - (1-\omega^2) u(\phi_A) + \omega^2 = 0$$

in the non-contacting region as $\omega \uparrow \sqrt{K}$. Since we must enforce both the contact condition (i.e., $u(\phi_A) = \sec\phi_A - 1$) as well as the slope condition (i.e., $u_\phi(\phi_A) = \sec\phi_A \tan\phi_A$) on the endpoint ϕ_A, we find that $P(\phi_A)$ does become exactly zero at the critical speed $\omega = \sqrt{K}$. For higher speeds, it is natural to assume that $P(\phi_A)$ stays zero (since P cannot be negative). We thus impose the additional boundary condition $P(\phi_A) = 0$ for $\omega^2 > K$.

In summary, above the critical speed, we retain the old boundary conditions of continuity of displacements at ϕ_A and ϕ_B, drop the requirement of slope continuity at ϕ_B, and use slope as well as curvature continuity at ϕ_A.

A.2. BEHAVIOR FAR FROM THE CRITICAL SPEED

The boundary conditions proposed above for the case of zero shear damping were derived using arguments that apply close to the critical speed. For the tire rotating at speeds *not* too close to the critical speed, we can justify the same boundary conditions by considering the case of zero shear damping to be the limiting case of small shear damping. To this end, we rewrite the five boundary conditions of equations (16) and (17) separately as follows:

$$\frac{\omega^2}{1-\omega^2} + C_1 e^{r_1 \phi_A} + C_2 e^{r_2 \phi_A} + C_3 e^{r_3 \phi_A} = \sec \phi_A - 1, \tag{A.2}$$

$$\frac{\omega^2}{1-\omega^2} + C_1 e^{r_1 \phi_B} + C_2 e^{r_2 \phi_B} + C_3 e^{r_3 \phi_B} = \sec \phi_B - 1, \tag{A.3}$$

$$r_1 C_1 e^{r_1 \phi_A} + r_2 C_2 e^{r_2 \phi_A} + r_3 C_3 e^{r_3 \phi_A} = \sec \phi_A \tan \phi_A, \tag{A.4}$$

$$r_1 C_1 e^{r_1 \phi_B} + r_2 C_2 e^{r_2 \phi_B} + r_3 C_3 e^{r_3 \phi_B} = \sec \phi_B \tan \phi_B, \tag{A.5}$$

$$r_1^2 C_1 e^{r_1 \phi_A} + r_2^2 C_2 e^{r_2 \phi_A} + r_3^2 C_3 e^{r_3 \phi_A} = \sec \phi_A \tan^2 \phi_A + \sec^3 \phi_A. \tag{A.6}$$

Recall from equation (14) that sufficiently far from critical speed $r_{1,2}$ are bounded, while r_3 is $\mathcal{O}(1/\zeta_2)$. Moreover, as $\zeta_2 \to 0^+$, the roots $r_{1,2}$ are bounded, while r_3 is $\mathcal{O}(1/\zeta_2)$. Moreover, as $\zeta_2 \to 0^+$, the roots $r_{1,2}$ approach the roots of the unperturbed quadratic equation (7). Finally, note that r_3 is negative below the critical speed and positive above the critical speed.

First consider the case below the critical speed. In this case, since $C_3 e^{r_3 \phi_B}$ is exponentially small compared to $C_3 e^{r_3 \phi_A}$, it can be dropped with negligible error from equations (A.3) and (A.5), giving (respectively)

$$\frac{\omega^2}{1-\omega^2} + C_1 e^{r_1 \phi_B} + C_2 e^{r_2 \phi_B} = \sec \phi_B - 1$$

and

$$r_1 C_1 e^{r_1 \phi_B} + r_2 C_2 e^{r_2 \phi_B} = \sec \phi_B \tan \phi_B.$$

Meanwhile, solving equation (A.6) for $C_3 e^{r_3 \phi_A}$, we find that it is an $\mathcal{O}(1/r_3^2) = \mathcal{O}(\zeta_2^2)$ quantity. Thus, dropping it from equations (A.2) and (A.4) to obtain

$$\frac{\omega^2}{1-\omega^2} + C_1 e^{r_1 \phi_A} + C_2 e^{r_2 \phi_A} = \sec \phi_A - 1$$

and

$$r_1 C_1 e^{r_1 \phi_A} + r_2 C_2 e^{r_2 \phi_A} = \sec \phi_A \tan \phi_A$$

introduces $\mathcal{O}(\zeta_2^2)$ and $\mathcal{O}(\zeta_2)$ errors, respectively. The four preceding equations can be solved for the four unknowns $C_{1,2}$ and $\phi_{A,B}$ with $\mathcal{O}(\zeta_2)$ error; and as $\zeta_2 \to 0^+$, we obtain exactly the boundary conditions presented earlier for the case of zero shear damping and below critical speed (equations (10) and (11)).

Now consider the case above critical speed. In this case, since $C_3 e^{r_3 \phi_A}$ is exponentially small compared to $C_3 e^{r_3 \phi_B}$, it can be dropped with negligible error from equations (A.2), (A.4) and (A.6), giving (respectively)

$$\frac{\omega^2}{1-\omega^2} + C_1 e^{r_1 \phi_A} + C_2 e^{r_2 \phi_A} = \sec \phi_A - 1,$$

$$r_1 C_1 e^{r_1 \phi_A} + r_2 C_2 e^{r_2 \phi_A} = \sec \phi_A \tan \phi_A$$

and

$$r_1^2 C_1 e^{r_1 \phi_A} + r_2^2 C_2 e^{r_2 \phi_A} = \sec \phi_A \tan^2 \phi_A + \sec^3 \phi_A.$$

Meanwhile, solving equation (A.5) for $C_3 e^{r_3 \phi_B}$, we find that it is an $\mathcal{O}(1/r_3) = \mathcal{O}(\zeta_2)$ quantity. Thus, dropping it from equation (A.3) to obtain

$$\frac{\omega^2}{1-\omega^2} + C_1 e^{r_1 \phi_B} + C_2 e^{r_2 \phi_B} = \sec \phi_B - 1,$$

introduces an $\mathcal{O}(\zeta_2)$ error. The four preceding equations can be solved for the four unknowns $C_{1,2}$ and $\phi_{A,B}$ with $\mathcal{O}(\zeta_2)$ error; and as $\zeta_2 \to 0^+$, we obtain exactly the boundary conditions presented earlier for the case of zero shear damping and above critical speed (equation (12)).

Note from the preceding calculations that, below *and* above critical speed, the third exponential term $C_3 e^{r_3 \phi}$ is at most $\mathcal{O}(\zeta_2)$ at one boundary and exponentially smaller away from that boundary. Thus, we can safely drop this term altogether in the limit as $\zeta_2 \to 0^+$.

We thus conclude the following for the tire with infinitesimally small shear damping and not close to critical speed: the two bounded roots of the characteristic equation $r_{1,2}$, the coefficients $C_{1,2}$ of the corresponding exponential functions, and the boundary points $\phi_{A,B}$ are the same as for the zero shear damping case; the contribution from the third exponential term is infinitesimal; and the boundary conditions determining $C_{1,2}$ and $\phi_{A,B}$ converge exactly to the same boundary conditions as used for the zero shear damping case.

We thus conclude that the boundary conditions used for zero shear damping, though motivated by consideration of speeds close to critical speed, are actually valid even far from critical speed.

A.3. PHYSICAL JUSTIFICATION IN A SIMPLE LIMITING CASE

The boundary conditions used for zero shear damping have been justified above using asymptotic arguments. Moreover, these boundary conditions are consistent with experimental observations as well (see Figure 12 and discussion in Section 5.2.2).

Here, as an aid to intuition that might complement the preceding asymptotic arguments, we present a purely physical argument in a simple limiting case.

Let us reconsider the system shown schematically in Figure 9, for the special case where the shear stiffness and damping are both zero (hence, $K = 0$). Then, for *any* non-zero rotation speed, $\omega^2 > K$, i.e., any rotation speed is above critical speed. As the system rotates, each mass point has a plastic collision with the ground at the leading edge ϕ_B, giving rise to a concentrated force at that point in the continuum limit. At the trailing edge ϕ_A, each mass point lifts off the ground only when the contact force becomes zero. Furthermore, on losing contact with the ground, each mass point in the $K = 0$ case executes radial oscillations. In lab-fixed co-ordinates, these are seen as a standing wave in the rotating tire, with spatial frequency inversely proportional to ω (i.e., decreasing with rotation rate, as observed in experiments on the tire).

Note that for this particularly simple limiting example, it is clear that the shock at the leading edge of contact coincides with the appearance of, but does not cause, the standing wave. It is also clear that the standing wave pattern formed on the tire is a result of free oscillations whose amplitude is determined by the geometry of the trailing contact edge, and so is not caused by resonance either.